

## RESEARCH ARTICLE

View Article Online  
View Journal | View IssueCite this: *Mater. Chem. Front.*,  
2023, 7, 964

# Interfacial engineering between SnO<sub>2</sub>/MAPbI<sub>3</sub> by maleate pheniramine halides toward carbon counter electrode-based perovskite solar cells with 16.21% efficiency†

Duoling Cao,<sup>‡a</sup> Zuhong Li,<sup>‡a</sup> Wenbo Li,<sup>a</sup> Ke Pei,<sup>a</sup> Xu Zhang,<sup>\*a</sup> Li Wan,<sup>id \*a</sup>  
Li Zhao,<sup>id a</sup> Alexey Cherevan,<sup>id b</sup> Dominik Eder<sup>id b</sup> and Shimin Wang<sup>\*a</sup>

Carbon counter electrode-based perovskite solar cells (C-PSCs) are considered among the most promising solar cells due to their excellent stability and low cost. However, the device performance is still unsatisfactory because of numerous defects at the interface between the electron transport layer (ETL) and perovskite (PVK) layer. In this work, we used two novel pheniramine halides containing maleic acid (*i.e.*, chlorphenamine maleate (CHM) and brompheniramine maleate (BHM)) to modify the SnO<sub>2</sub>/MAPbI<sub>3</sub> interface. All modifiers can passivate interface defects, reduce interface strain, and enhance device performance. As a result, the champion power conversion efficiency (PCE) values of HTL-free C-PSCs modified with CHM and BHM are 15.47% and 16.21%, respectively, which are much higher than the 13.45% of the control device. Moreover, the unencapsulated BHM-modified device maintains approximately 82.7% of its initial PCE under ambient conditions with 35% relative humidity at room temperature for 800 h. This study provides a new idea for the application of multifunctional complex molecules in high-efficiency and stable C-PSCs.

Received 9th November 2022,  
Accepted 14th January 2023

DOI: 10.1039/d2qm01149b

rsc.li/frontiers-materials

## 1. Introduction

In the past decade, organic–inorganic hybrid perovskite solar cells (PSCs) have received extensive attention from scholars, with the power conversion efficiency (PCE) significantly improving from 3.8% to 25.7%.<sup>1–4</sup> Unfortunately, high-efficiency devices contain an organic hole transporting layer (HTL) and precious metal electrodes, which increase the cost and energy consumption and complicate the manufacturing steps.<sup>5,6</sup> Recent studies have shown that metal corrosion adversely affects the performance and stability of the PSCs.<sup>7</sup> Therefore, HTL-free carbon counter electrode-based PSCs (C-PSCs) have become one of the most promising alternatives owing to their low raw material cost

and simple manufacturing process.<sup>8–10</sup> Recently, Ye *et al.* obtained the highest PCE of 18.9% in C-PSCs without a HTL.<sup>11</sup> Despite all the progress, C-PSCs suffer from serious energy losses caused by the high resistance of the carbon counter electrode (CE), poor interface contact between the carbon CEs, and quality of the electron transport layer (ETL) and the perovskite layer.<sup>12–14</sup>

The ETL and perovskite film are also crucial to the performance and stability of PSCs, except for the influence of conductive carbon paste.<sup>4,15,16</sup> Generally, tin oxide (SnO<sub>2</sub>) is commonly used as an ETL in PSCs due to the advantages of low-temperature processing, high transmittance, excellent chemical stability and low photocatalytic activity.<sup>17,18</sup> However, the interfacial energy between SnO<sub>2</sub> and the perovskite can hinder the charge extraction and transfer, leading to severe charge recombination.<sup>19–21</sup> In particular, the undercoordinated Sn<sup>4+</sup> and –OH groups on the SnO<sub>2</sub> surface could seriously affect the contact between SnO<sub>2</sub> and the perovskite, resulting in the degradation of the quality of the perovskite film and the performance of the PSCs.<sup>22</sup>

Various functional materials have been developed to regulate the energy alignment of the SnO<sub>2</sub> and passivate the surface defects, mainly including inorganic or organic salts,<sup>21,23,24</sup> Lewis acid and base molecules,<sup>25</sup> polymers, and quantum dots.<sup>19,26,27</sup> Among them, carboxyl (–O–C=O)<sup>28–30</sup> and halide (–Cl,<sup>31,32</sup> –Br,<sup>33</sup> *etc.*) groups can coordinate with the

<sup>a</sup> Key Laboratory for the Green Preparation and Application of Functional Materials, Ministry of Education, Hubei Key Laboratory of Polymer Materials, Hubei Collaborative Innovation Center for Advanced Organic Chemical Materials, Faculty of Materials Science and Engineering, Hubei University, Wuhan 430062, P. R. China. E-mail: xuzhang@hubu.edu.cn, wanli@hubu.edu.cn, wanli1983\_3@aliyun.com, shiminwang@126.com

<sup>b</sup> Institute of Materials Chemistry, Technische Universität Wien, Getreidemarkt 9/165, 1060 Vienna, Austria

† Electronic supplementary information (ESI) available: Details of materials, device fabrications, and characterization. See DOI: <https://doi.org/10.1039/d2qm01149b>

‡ These authors contributed equally.

undercoordinated interfacial metal atoms, such as Sn and Pb, to regulate the energy levels of SnO<sub>2</sub>, passivate the defect density at the SnO<sub>2</sub>/perovskite interface, and ultimately improve the device performance.

For example, Chen *et al.* found that 4-imidazoleacetic acid hydrochloride (ImAchCl) can be used as a passivation layer at the SnO<sub>2</sub>/perovskite interface in planar PSCs because it can passivate the interface defects by reactions with the hydroxyl group (–OH) on the SnO<sub>2</sub> surface.<sup>28</sup> Diao *et al.* used maleic anhydride to improve the efficiency and stability of PSCs, and its hydrolysate (maleic acid) can also act as a passivator for perovskites. The perovskite film would become more compact and smooth due to the interaction between carboxyl groups (C=O) and the undercoordinated Pb<sup>2+</sup>.<sup>34</sup> In addition, Dong *et al.* used 2,4,5-trichlorobenzenesulfonic acid potassium salt (3Cl-BSAK) as a functional ETL, and the undercoordinated Sn on the surface of the SnO<sub>2</sub> film was efficiently passivated with the Cl in 3Cl-BSAK.<sup>35</sup> Xiong *et al.* reported that biguanide hydrochloride (BGCl) was chemically linked to the SnO<sub>2</sub> film *via* Lewis coordination or electrostatic coupling to enhance electron extraction.<sup>36</sup> Zhang *et al.* used the strong interaction between F<sup>–</sup> ions or C=O groups in potassium trifluoroacetate (KTFA) and Sn<sup>2+</sup> or Pb<sup>2+</sup> to improve the quality of the SnO<sub>2</sub> and perovskite films, passivate the interface defects, and suppress ion migration.<sup>37</sup> These works demonstrate that adding appropriate multifunctional modification molecules to the SnO<sub>2</sub>/perovskite interface can improve the quality of the SnO<sub>2</sub> films and passivate the interface defects. Consequently, designing and developing more efficient multifunctional interface modifiers are greatly important to further improve the PCE and stability of C-PSCs.

Herein, we demonstrate a multifunctional interfacial modification strategy using two novel maleate pheniramine halides (CHM and BHM) to modify the interface between SnO<sub>2</sub> and the perovskite. The two maleate pheniramine halides can interact with the –OH in SnO<sub>2</sub> and undercoordinated Pb<sup>2+</sup> in the perovskite; thus, the interface between them could be stabilized. Moreover, the Cl– or Br– groups in the benzene ring can form Sn–X bonds with the Sn atoms in the SnO<sub>2</sub> ETL, thereby effectively reducing dangling bonds on the surface. Furthermore, the device based on BHM exhibits a lower trap density and a higher PCE than the device based on CHM. Finally, the device based on BHM attains a PCE as high as 16.21%, with much improved stability under ambient conditions.

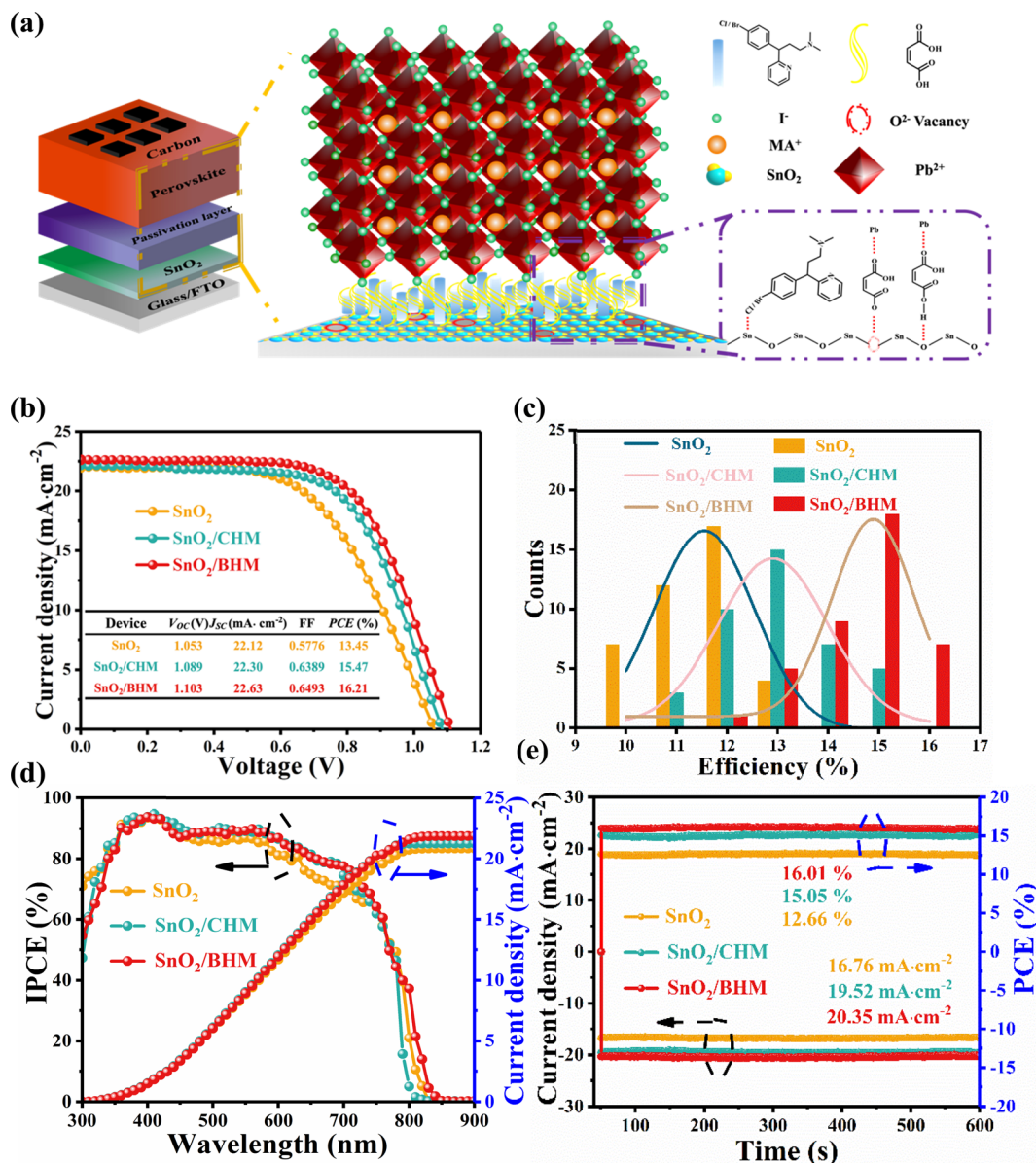
## 2. Results and discussion

Fig. S1 (ESI<sup>†</sup>) shows the 2D molecular structures and 3D conformer schematics of CHM and BHM. The PSCs are fabricated in the FTO/SnO<sub>2</sub>/MAPbI<sub>3</sub>/carbon architecture. The CHM and BHM are used as interface passivation layers to modify the SnO<sub>2</sub>/MAPbI<sub>3</sub> interface (Fig. 1a). On the one hand, the C=O in CHM or BHM can be esterified with –OH on the surface of the SnO<sub>2</sub> film to passivate the defects and avoid the oxidative decomposition of SnO<sub>2</sub>, thereby improving the device stability.<sup>38</sup>

On the other hand, the electron-donating C=O on CHM or BHM can interact with the undercoordinated Pb<sup>2+</sup> ions in the MAPbI<sub>3</sub> perovskite, promoting the crystallization of the perovskite and passivating the film defects.<sup>25,33,36</sup> In addition, the halogen atoms on the benzene ring act as a Lewis base to passivate the undercoordinated Sn on the surface of the SnO<sub>2</sub> film, which can enhance the carrier transport at the interface of the ETL and the perovskite layer.

We initially systematically compare the effects of two modifier on the photovoltaic performance of the device, as shown in Fig. S2 and S3 (ESI<sup>†</sup>) with the statistics listed in Table S1 and S2 (ESI<sup>†</sup>). The devices exhibit the best performance when the amount of CHM and BHM is 18 and 20 mg mL<sup>–1</sup>, respectively. Fig. 1b shows the photoinduced photocurrent density–voltage (*J–V*) curves of PSCs using different maleate pheniramine halide modifier, including key parameters such as the short-circuit current density (*J*<sub>sc</sub>), open-circuit voltage (*V*<sub>oc</sub>), fill factor (FF), and PCE summarized in Table S3 (ESI<sup>†</sup>) (the record PCE of the state-of-the-art HTL-free CE-based MAPbI<sub>3</sub> PSCs is shown in Table S4, ESI<sup>†</sup>). The PSCs based on CHM (18 mg mL<sup>–1</sup>) show a PCE of 15.47%, with a *V*<sub>oc</sub> of 1.089 V, a *J*<sub>sc</sub> of 22.30 mA cm<sup>–2</sup>, and a FF of 0.639. With the introduction of BHM (20 mg mL<sup>–1</sup>) in the ETL, the PCE is increased to 16.21%, with a *V*<sub>oc</sub> of 1.103 V, a *J*<sub>sc</sub> of 22.63 mA cm<sup>–2</sup>, and a FF of 0.649. Compared with CHM based devices, the *V*<sub>oc</sub> of the BHM based device is significantly increased from 1.087 ± 0.01 V to 1.104 ± 0.01 V. Interestingly, the significant increase in efficiency is mainly attributed to the improvement in *V*<sub>oc</sub>, which may be related to the decrease in non-radiative recombination of defects at the interface between the ETL and the perovskite. As shown in Fig. 1c and Fig. S4 (ESI<sup>†</sup>), 40 individual devices were subsequently fabricated to characterize consistency and reproducibility. The incident photon-to-electron conversion efficiency (IPCE) and the integrated *J*<sub>sc</sub> for the champion devices are plotted in Fig. 1d. The corresponding integrated *J*<sub>sc</sub> values of SnO<sub>2</sub>, SnO<sub>2</sub>/CHM, and SnO<sub>2</sub>/BHM ETL-based devices were 20.85, 21.27, and 21.88 mA cm<sup>–2</sup>, respectively, which were consistent with the *J*<sub>sc</sub> values from the *J–V* results. Subsequently, we measured the steady-state power output (SPO) of the best performing devices of each substrate for 100 seconds at a fixed voltage near the maximum power point (MPP) obtained from the peak *J–V* curves (Fig. 1e).<sup>39</sup> The device based on untreated SnO<sub>2</sub> possessed an output current density of 16.76 mA cm<sup>–2</sup> and an output PCE of 12.66%, whereas the CHM-modified device (19.52 mA cm<sup>–2</sup> and 15.05%) and BHM-modified device (20.35 mA cm<sup>–2</sup> and 16.01%) produced a higher current density and PCE at the same time.

X-ray photoelectron spectroscopy (XPS) measurement is used to analyze the surface chemical properties of SnO<sub>2</sub>, SnO<sub>2</sub>/CHM, and SnO<sub>2</sub>/BHM films.<sup>40</sup> The full scan XPS spectra are presented in Fig. S5a (ESI<sup>†</sup>). The CHM/SnO<sub>2</sub> and BHM/SnO<sub>2</sub> films show several additional peaks located at *ca.* 401.5 eV and 398.8 eV, respectively, ascribed to the N 1s peak (Fig. S5b, ESI<sup>†</sup>), C–N, and O–C=O (Fig. 2a) contrary to the pristine SnO<sub>2</sub>, indicating the combination of CHM/BHM and the SnO<sub>2</sub>. Meanwhile, the Sn 3d<sub>3/2</sub> and 3d<sub>5/2</sub> peaks from BHM/SnO<sub>2</sub> and CHM/



**Fig. 1** (a) Schematic illustration of the formation of the BHM or CHM passivation layer between SnO<sub>2</sub> and the perovskite layer. (b) J–V curves of devices (0.06 cm<sup>2</sup>) based on SnO<sub>2</sub> (orange), SnO<sub>2</sub>/CHM (cyan), and SnO<sub>2</sub>/BHM (red) under AM 1.5 G illumination. The scan rate is 0.1 V s<sup>-1</sup>. (c) Statistical diagrams of the parameters including the PCE of the PSCs based on SnO<sub>2</sub> and SnO<sub>2</sub> modified by CHM and BHM calculated from individual 40 devices. (d) The IPCE spectra and the corresponding integrated J<sub>SC</sub> of the champion devices of PSCs based on different ETL layers. (e) The stabilized power output of the champion devices and current density measured as a function of time for the devices based on SnO<sub>2</sub>, SnO<sub>2</sub>/CHM and SnO<sub>2</sub>/BHM biased at the maximum power point at 0.756, 0.771 and 0.787 V bias, respectively.

SnO<sub>2</sub> are shifted to higher binding energies than the pristine SnO<sub>2</sub> in Fig. 2b. This finding is mainly attributed to the electrostatic coupling interaction of halogen atoms in pheniramine halides with Sn atoms in SnO<sub>2</sub>.<sup>35,41</sup> This result is further supported by the formation of Sn–X bonds (Fig. S5c and d, ESI<sup>†</sup>), leading to the enhanced electron extraction capability of ETLs. Additionally, it can be determined that BHM bound more strongly to SnO<sub>2</sub> than CHM by calculating the CHM and BHM complexation energies with SnO<sub>2</sub> (Fig. S6, ESI<sup>†</sup>). The O 1s for pure SnO<sub>2</sub> film displays two distinct peaks at 530.29 and 531.40 eV, corresponding to the Sn–O bond (lattice oxygen, O<sub>L</sub>)

in SnO<sub>2</sub> and the oxygen vacancies (O<sub>V</sub>) or surface absorbed hydroxyl groups (O<sub>OH</sub>), respectively (Fig. 2c).<sup>35,38</sup> Both groups moved to a higher binding energy after CHM (530.43 eV for O<sub>L</sub> and 531.70 eV for O<sub>V</sub> or O<sub>OH</sub>) and BHM (530.66 eV for O<sub>L</sub> and 531.90 eV for O<sub>V</sub> or O<sub>OH</sub>) treatments, indicating the esterification reaction between –OH at the surface of the SnO<sub>2</sub> film and –COOH of CHM or BHM. Fig. 2d evidently shows that the two distinct peaks of 143.31 and 138.44 eV that belong to Pb 4f<sub>5/2</sub> and Pb 4f<sub>7/2</sub> in the PbI<sub>2</sub> film, respectively, are also shifted to lower binding energies after CHM (143.09 eV and 138.21 eV) and BHM (143.01 eV and 138.13 eV) modification. The peak

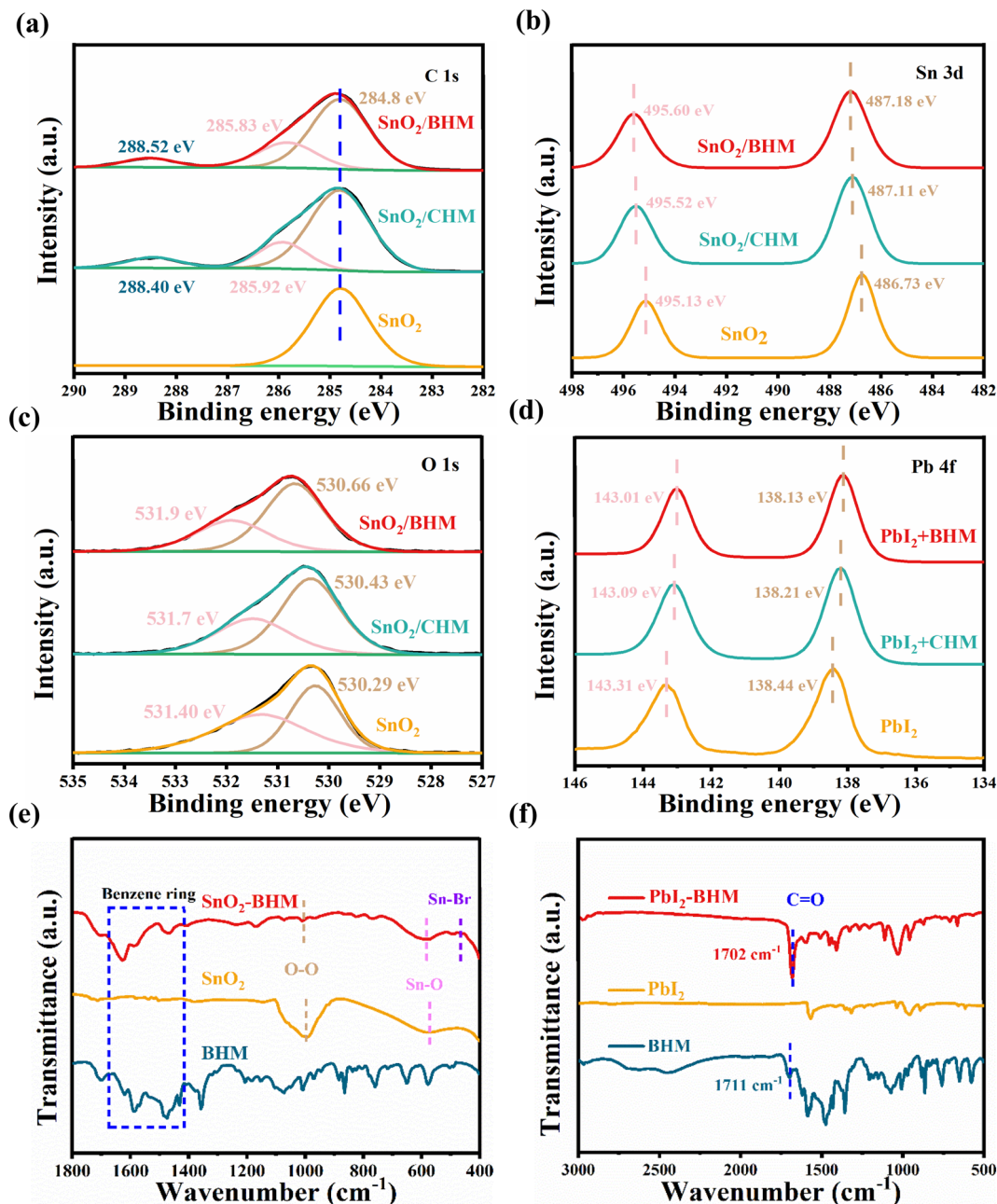


Fig. 2 XPS spectra of (a) C 1s, (b) Sn 3d, and (c) O 1s for unmodified SnO<sub>2</sub>, SnO<sub>2</sub>/CHM and SnO<sub>2</sub>/BHM, where the peak was deconvoluted showing background (blue lines), measured data (black lines) and fitted peaks (magenta, grey and olive). (d) The XPS spectra of Pb 4f from the PbI<sub>2</sub>, BHM, and PbI<sub>2</sub>-BHM films. (e) FTIR spectra of film samples of SnO<sub>2</sub>, BHM, and the mixtures SnO<sub>2</sub>-BHM in the range of 1800 to 400 cm<sup>-1</sup>. (f) FTIR spectra of film samples of PbI<sub>2</sub>, BHM, and PbI<sub>2</sub>-BHM in the range of 3000 to 500 cm<sup>-1</sup>.

shifts of C=O and O-C=O, and the appearance of the new peak of the Pb-O bond in modified films, further confirm the chemical interaction between O-C=O and C=O in the CHM or BHM and undercoordinated Pb<sup>2+</sup>, as expected in the O1s XPS spectra (Fig. S7, ESI†).<sup>37</sup>

The FTIR results in Fig. 2e show that in contrast to unmodified SnO<sub>2</sub>, three characteristic peaks at *ca.* 1596, 1481, and 1465 cm<sup>-1</sup> in the modified films are due to benzene rings in the BHM, indicating the existence of BHM in the SnO<sub>2</sub> films (Fig. S8, ESI†). For the BHM/SnO<sub>2</sub> film, the peaks belonging

to the Sn-O vibration shift from 562 to 579 cm<sup>-1</sup>, suggesting the interaction between the -OH in SnO<sub>2</sub> and -COOH in BHM. Furthermore, the peak at 1046 cm<sup>-1</sup> in the SnO<sub>2</sub> film can be ascribed to the stretching vibrations of the O-O in the ion-radical forms of adsorbed oxygen of type O<sub>2</sub><sup>-</sup> on the SnO<sub>2</sub> surface.<sup>42</sup> A weak absorption peak at 1072 cm<sup>-1</sup> is observed after the BHM treatment, which may also be due to the esterification. The peaks at 447 and 459 cm<sup>-1</sup> belong to Sn-Cl and Sn-Br vibrations in the modified film (Fig. S9a, ESI†), respectively. These results can further demonstrate the

existence of CHM and BHM, consistent with the XPS results. Fig. 2f and Fig. S9b (ESI†) show the FTIR spectra of PbI<sub>2</sub>, BHM (CHM), and PbI<sub>2</sub>-BHM (PbI<sub>2</sub>-CHM) films. The results indicate that the interaction between BHM and the perovskite is ascribed to the chemical affinity of Pb<sup>2+</sup> with the maleate acid group. An additional peak at around 1700 cm<sup>-1</sup> is due to the C=O stretching vibration in the PbI<sub>2</sub>-BHM or PbI<sub>2</sub>-CHM film.<sup>23,30</sup> Meanwhile, the characteristic peaks of the C=O stretching vibration in CHM (1706 cm<sup>-1</sup>) and BHM (1702 cm<sup>-1</sup>) shift to 1710 cm<sup>-1</sup> (CHM) and 1711 cm<sup>-1</sup> (BHM), further demonstrating the chemical interaction between the maleate acid group in the maleate pheniramine halides and undercoordinated Pb<sup>2+</sup> or Pb clusters in the perovskite.

We measured the conductivity of various ETLs with the device structure of FTO/ETL/Au. The conductivity of the ETL is related to the slope of the current–voltage (*I*–*V*) curve. As shown in Fig. 3a, the SnO<sub>2</sub>/CHM and SnO<sub>2</sub>/BHM show a larger slope than the pure SnO<sub>2</sub>, suggesting that the film conductivity was slightly improved after CHM and BHM treatments, which is likely to be beneficial for electron transfer.<sup>43</sup> The optical transmission spectra of SnO<sub>2</sub>, SnO<sub>2</sub>/CHM, and SnO<sub>2</sub>/BHM are shown in Fig. 3b. These films show high transmittance in the visible region, indicating excellent optical quality. Acquired from the UV visible spectra (Fig. S10, ESI†), the bandgap (*E*<sub>g</sub>) of the SnO<sub>2</sub> and SnO<sub>2</sub> modified films is the same at 3.85 eV. The absorption spectra in Fig. 3c also show that the CHM or BHM treatment has a negligible effect on the perovskite films. The films without and with modification by CHM and BHM exhibit the same bandgap of 1.60 eV in Fig. S11 (ESI†).

Ultraviolet photoelectron spectroscopy (UPS) measurement is performed to investigate the energy band structure of ETLs.<sup>22,27</sup> The conduction band minimum (*E*<sub>c</sub>) and valence band maximum (*E*<sub>v</sub>) without and with CHM and BHM modification are calculated using the energy cutoff (*E*<sub>cutoff</sub>) region (Fig. 3d) and the energy onset (*E*<sub>onset</sub>) region (Fig. 3e). Fig. 3f illustrates the energy band alignment between the ETLs and perovskite. In the equation of *E*<sub>v</sub> = *E*<sub>cutoff</sub> – *E*<sub>onset</sub> – *hν*, where *hν* is the energy of the He α ultraviolet photon source. We calculated the *E*<sub>v</sub> to be –8.27, –8.14, and –8.09 eV for SnO<sub>2</sub>, SnO<sub>2</sub>/CHM and SnO<sub>2</sub>/BHM, respectively. We then calculated the *E*<sub>c</sub> of SnO<sub>2</sub>, SnO<sub>2</sub>/CHM, and SnO<sub>2</sub>/BHM samples at –4.42, –4.29, and –4.24 eV from *E*<sub>c</sub> = *E*<sub>v</sub> + *E*<sub>g</sub>, respectively. After modification, the VBM and CBM of SnO<sub>2</sub> are closer to the conduction band and valence band of the perovskite. As a result, the interface energy barrier is reduced, and interface recombination is inhibited to improve the *V*<sub>OC</sub> of the devices. Furthermore, in contrast to the CHM/SnO<sub>2</sub>, the energy band alignment of BHM/SnO<sub>2</sub> is closer to the perovskite, which is one of the reasons for the better photovoltaic performance of the corresponding devices.

The effect of different ETLs on the quality of perovskite films was investigated by X-ray diffraction (XRD). In Fig. 4a, the relatively sharp peaks at 14.263°, 28.584° and 32.031° correspond to the (110) (220) and (310) planes of the perovskite for all samples.<sup>44</sup> This finding indicates that the addition of BHM

and CHM in SnO<sub>2</sub> has slight effects on the structure of the perovskite. Fig. 4b demonstrates the full width at half maximum (FWHM) for the (110) peak of perovskite films with various ETLs. Therefore, the modified ETLs have a favorable effect on the crystallinity of the perovskite film due to the significant decrease in the FWHM. The contact angles of SnO<sub>2</sub>, SnO<sub>2</sub>/CHM, and SnO<sub>2</sub>/BHM shown in Fig. 4c are 17.5°, 14.5°, and 12.0°, respectively. The smaller contact angle results in the wettability interface for the perovskite.<sup>45</sup> Therefore, the small contact angle of the ETLs could provide a low surface energy,<sup>46</sup> which is probably responsible for the improved crystallinity of the perovskite coated on the BHM/SnO<sub>2</sub> ETL.<sup>21,47</sup> Fig. 4d shows the top-view scanning electron microscopy (SEM) images of the perovskite films deposited on different ETLs, including SnO<sub>2</sub>, SnO<sub>2</sub>/CHM, and SnO<sub>2</sub>/BHM. The images clearly show that compact and dense surface morphologies were obtained. Compared with the perovskite film deposited on the pure SnO<sub>2</sub> substrates, the CHM or BHM modified perovskite films have a more uniform morphology, larger grains, and fewer grain boundaries. Fig. S12 (ESI†) shows the distribution diagram with an average grain size of the perovskite spin-coated on ETLs. The grain size is increased from 289 nm to 473 nm for the BHM-modified sample. Fig. S13 (ESI†) shows the cross-sectional SEM images of the complete solar cell structure. The perovskite film is approximately 650 nm. The grains of the perovskite film coated on the BHM/SnO<sub>2</sub> substrate are sufficiently large enough to penetrate through the film thickness, without any pinhole. The result is consistent with the top-view SEM images.

We estimated the recombination dynamics in different ETLs by photoluminescence (PL) and time-resolved photoluminescence (TRPL) spectroscopy.<sup>48</sup> The prominent PL in the FTO/SnO<sub>2</sub>/BHM or CHM/perovskite in Fig. 5a indicates more efficient charge mobility after CHM or BHM treatment. Fig. 5b and Table S5 (ESI†) show the lifetime and average carrier lifetime (*τ*<sub>ave</sub>) of the TRPL spectra calculated by the equation  $I(t) = I_0 + A_1 \exp\left(-\frac{t}{\tau_1}\right) + A_2 \exp\left(-\frac{t}{\tau_2}\right)$ , and  $\tau_{ave} = \frac{A_1 \tau_1^2 + A_2 \tau_2^2}{A_1 \tau_1 + A_2 \tau_2}$ , where *A*<sub>1</sub> and *A*<sub>2</sub> are the amplitude of *τ*<sub>1</sub> and *τ*<sub>2</sub>, *I*<sub>0</sub> is a constant, and *τ*<sub>1</sub> and *τ*<sub>2</sub> are the fast and slow decay component, respectively.<sup>49</sup> The *τ*<sub>ave</sub> of the modified ETLs is only one third (90.23 ns for BHM/SnO<sub>2</sub>) or one half (178.48 ns for CHM/SnO<sub>2</sub>) of the original film (273.62 ns for SnO<sub>2</sub>). In addition, to illustrate that the modification of BHM and CHM inhibits the generation of perovskite defects, we constructed glass/BHM or CHM/perovskite film structure models. According to Table S6 and Fig. S14 (ESI†), compared with the *τ*<sub>ave</sub> of control samples (84.71 ns), the ones of the BHM (156.23 ns) and CHM (142.95 ns) modified samples show an obvious increase. These results suggest that the interface modification of CHM and BHM can effectively reduce the defects and improve the efficiency of electron extraction and transport between ETLs and the perovskite.

The space charge-limited current (SCLC) measurement was conducted to quantify the trap densities of the perovskite films coated on different ETLs. Fig. 5c, d and Fig. S15 (ESI†) show the dark *I*–*V* curves of the electron-only devices with a structure of

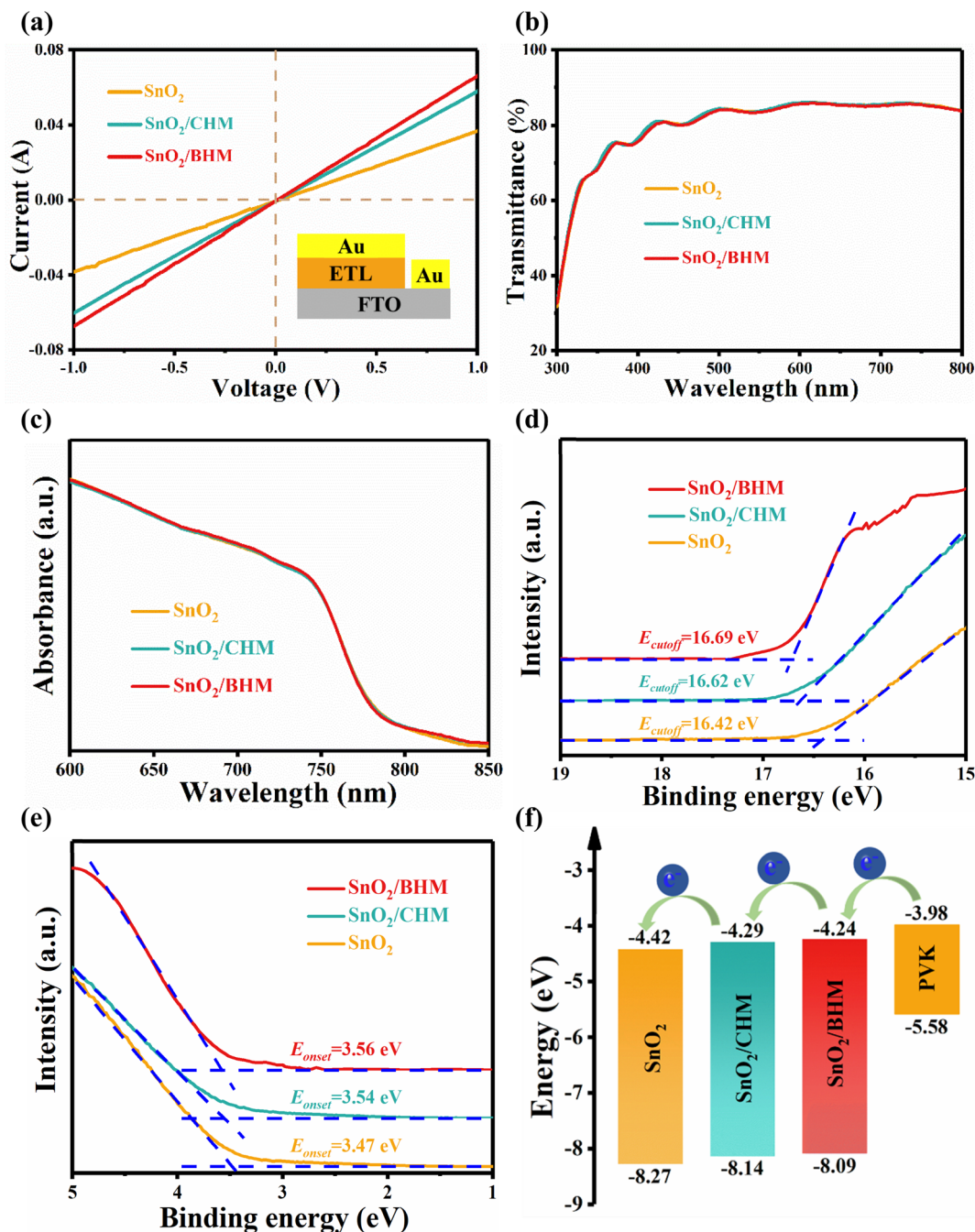
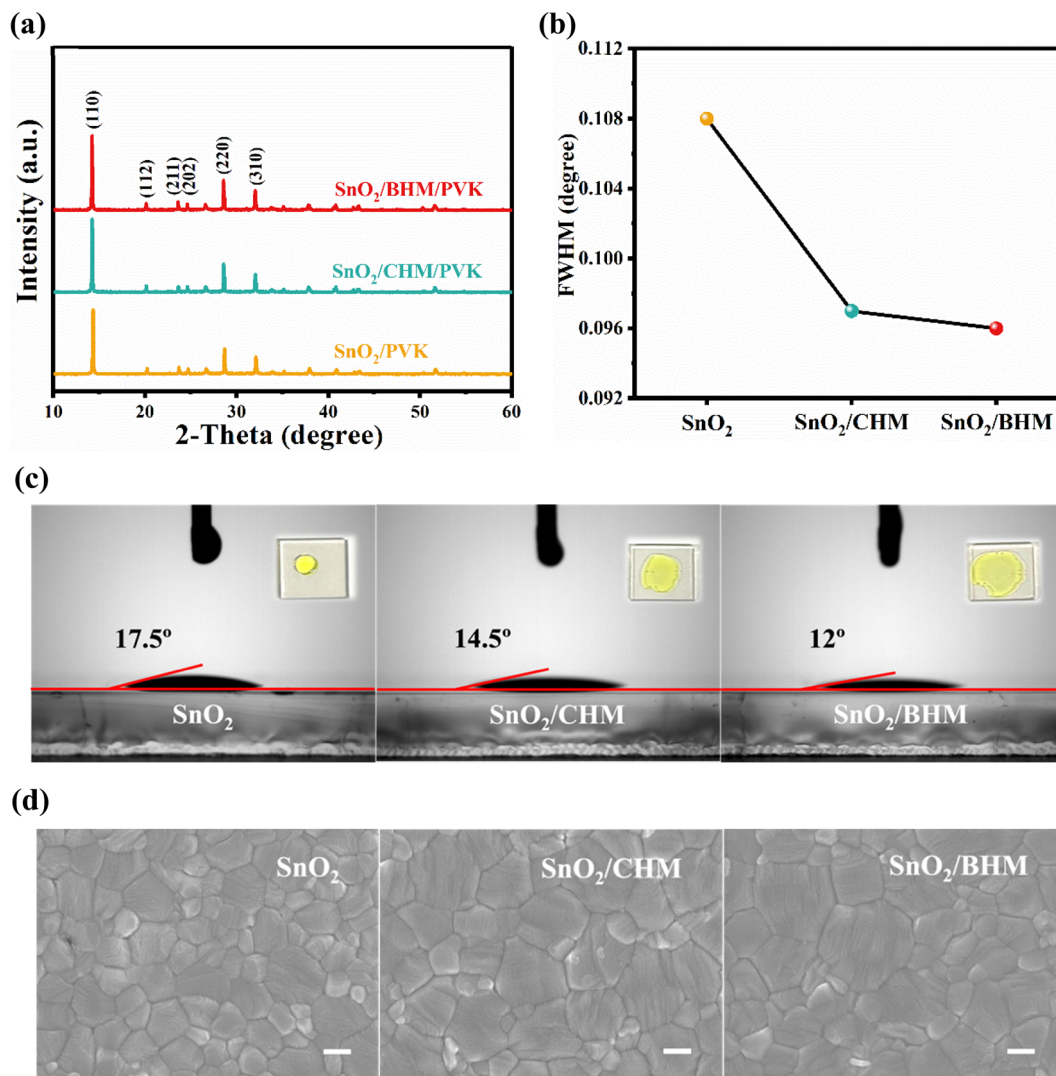


Fig. 3 (a) Conduction properties of various films under dark conditions. (b) Transmission spectra of the SnO<sub>2</sub> film and modified SnO<sub>2</sub> films. (c) Absorption spectra of perovskite films deposited on SnO<sub>2</sub> and modified SnO<sub>2</sub> films. (d) UPS spectra of the secondary electron cutoff region and (e) onset value energy for pristine SnO<sub>2</sub> and modified SnO<sub>2</sub> films. (f) Energy level diagram of SnO<sub>2</sub>, SnO<sub>2</sub>/CHM, SnO<sub>2</sub>/BHM, and the perovskite. The blue sphere represents photovoltaic electrons, and the green arrows refer to electronic transportation.

FTO/ETL/perovskite/PCBM/Ag. The  $I$ - $V$  curve has linear correlation at low bias voltage, showing an ohmic-type response. When the bias voltage exceeds the trap-filled limit voltage ( $V_{\text{TFL}}$ ), the current begins to increase nonlinearly, indicating that all the available trap states would be filled. The equation of the trap density ( $n_t$ ) is obtained as follows:

$$n_t = \frac{2\epsilon_0\epsilon_r V_{\text{TFL}}}{eL^2}$$

where  $\epsilon_0$  is the vacuum permittivity,  $\epsilon_r$  is the relative dielectric constant ( $\epsilon_r = 33.5$ ),<sup>50</sup>  $e$  is the electron charge, and  $L$  is the thickness of the perovskite film. The trap density of the perovskite film on SnO<sub>2</sub> ETLs is  $3.33 \times 10^{15} \text{ cm}^{-3}$ . Surprisingly, the trap density of the perovskite film on CHM/SnO<sub>2</sub> and BHM/SnO<sub>2</sub> ETL is reduced to  $2.28 \times 10^{15}$  and  $1.93 \times 10^{15} \text{ cm}^{-3}$ , respectively. The lowest trap density of the BHM/SnO<sub>2</sub> device is due to the low grain boundary



**Fig. 4** (a) XRD spectra of perovskite films deposited on the SnO<sub>2</sub> ETL and modified ETLs. (b) The dependence of FWHM on the (110) crystal plane of perovskite films with CHM or BHM treatment compared with pristine SnO<sub>2</sub> ETLs. (c) The contact angle measurements of perovskite precursor solution on FTO/SnO<sub>2</sub>, FTO/SnO<sub>2</sub>/CHM, and FTO/SnO<sub>2</sub>/BHM. (d) The SEM top-view images of perovskite films deposited on the SnO<sub>2</sub>, SnO<sub>2</sub>/CHM, SnO<sub>2</sub>/BHM substrates; the scale bar is 200 nm.

density in the perovskite film (Fig. 4d) and the strongest chemical interaction between the perovskites and the modified SnO<sub>2</sub> ETL (Fig. 2).<sup>33</sup>

Electrochemical impedance spectroscopy (EIS) is employed to gain deep insight into charge transfer and recombination.<sup>51</sup> Fig. S16 and Table S7 (ESI<sup>†</sup>) show the Nyquist plots of the devices with different ETLs. The series resistance ( $R_s$ ) of the SnO<sub>2</sub> is slightly increased after CHM and BHM treatment. In the EIS analysis, the high-frequency and low-frequency regions represent the charge transfer resistance ( $R_{tr}$ ) and recombination resistance ( $R_{rec}$ ), respectively. Compared with SnO<sub>2</sub> and SnO<sub>2</sub>/CHM-based PSCs, the SnO<sub>2</sub>/BHM-based device shows the smallest  $R_{tr}$  of 233.3  $\Omega$  and the largest  $R_{rec}$  of 2500  $\Omega$ , indicating the best film morphology, most efficient carrier transport and lowest recombination. Fig. 5e shows the dark current densities of the solar cells with different ETLs. It shows

a decreasing tendency with the CHM and BHM modification, which may be related to the improvement of carrier transport efficiency and the reduction of leakage current induced by charge recombination.<sup>52</sup>

Stability is one of the most important characteristics of PSCs. Fig. 5f shows the normalized PCE of the unencapsulated devices with different ETLs stored under ambient conditions with 35% relative humidity and room temperature. The CHM and BHM modified devices retain over 80% of their initial PCE after 800 h, but the device with SnO<sub>2</sub> only maintains ca. 30% of its initial PCE. This large gap indicates that the long-term stability of the device has been greatly improved after interfacial modification. This may be ascribed to the large grain size of the perovskite film, so the perovskite degradation at the grain boundary is inhibited, which ultimately leads to the improvement of device stability.

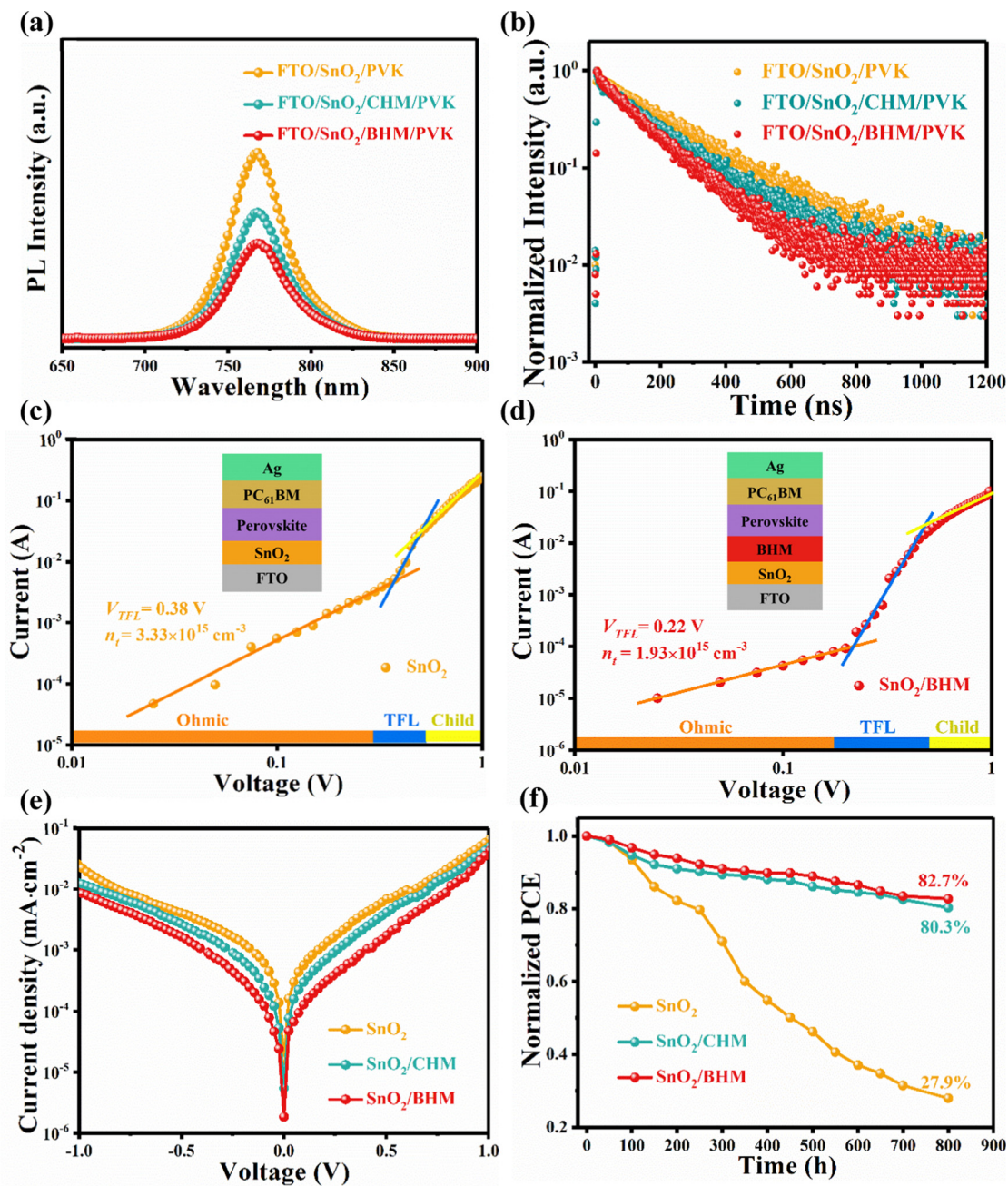


Fig. 5 (a) Steady-state PL spectrum of perovskite films deposited on  $\text{SnO}_2$  substrates without and with CHM or BHM modification. (b) TRPL attenuation transient spectrum of perovskite films on  $\text{SnO}_2$  (orange),  $\text{SnO}_2/\text{CHM}$  (cyan), and  $\text{SnO}_2/\text{BHM}$  (red) substrates. Dark  $I$ - $V$  curves of the electron-only devices with a configuration of (c)  $\text{FTO}/\text{SnO}_2/\text{MAPbI}_3/\text{PCBM}/\text{Au}$ , and (d)  $\text{FTO}/\text{SnO}_2/\text{BHM}/\text{MAPbI}_3/\text{PCBM}/\text{Au}$ . (e) Dark  $J$ - $V$  curves of the devices based on  $\text{SnO}_2$  (orange),  $\text{SnO}_2/\text{CHM}$  (cyan), and  $\text{SnO}_2/\text{BHM}$  (red). (f) The normalized PCE values of the corresponding unencapsulated PSCs in an ambient environment with 30% RH and 25 °C.

### 3. Conclusions

We developed an effective maleate pheniramine halide modified  $\text{SnO}_2$  ETL for the  $\text{MAPbI}_3$  perovskite solar cell and achieved an increased PCE of 16.21%. The excellent device performance is related to the larger grain size, better crystallinity, lower trap density and interface energy barrier of the  $\text{MAPbI}_3$  film deposited on  $\text{BHM}/\text{SnO}_2$ . Therefore, improved charge transfer efficiency and inhibited interface recombination are realized in the highly efficient devices. Meanwhile, the long-term stability is

significantly improved with the modified  $\text{SnO}_2$  ETL. We believe that this work has made great strides in developing high-quality electron transport layers, which will play an important role in promoting the progress of perovskite photovoltaics.

### Author contributions

Duoling Cao and Zuhong Li carried out experimental research, wrote the draft of manuscript, and participated in writing the



theoretical part of the manuscript. Wenbo Li provided help for the problems encountered in the experiment. Li Wan supervised the experimental research of the manuscript, revised the draft of manuscript. Li Zhao, Ke Pei and Alexey Cherevan helped revising the manuscript. Xu Zhang, Li Wan, Dominik Eder and Shimin Wang provided funding support.

## Conflicts of interest

There are no conflicts to declare.

## Acknowledgements

This work was supported by the NSFC (21402045), the Higher Education Discipline Innovation Project (“111 Project”, D18025), the Key Program for Intergovernmental S&T Innovation Cooperation Projects of National Key R&D Program of China (2019YFE0107100), and Austria/China Scientific & Technological Cooperation (WTZ-OeAD CN03/2020). This work was also financially supported by the Hubei Provincial Department of Education (D20181005), and the Department of Science & Technology of Hubei Province of China (2014CFB167 and 2022CFB981).

## References

- 1 NREL. Best Research-Cell Efficiency Chart, (accessed: August 2022), <https://www.nrel.gov/pv/cell-efficiency.html>.
- 2 A. Kojima, K. Teshima, Y. Shirai and T. Miyasaka, Organometal halide perovskites as visible-light sensitizers for photovoltaic cells, *J. Am. Chem. Soc.*, 2009, **131**, 6050–6051.
- 3 Y. Chen, S. Tan, N. Li, B. Huang, X. Niu, L. Li, M. Sun, Y. Zhang, X. Zhang, C. Zhu, N. Yang, H. Zai, Y. Wu, S. Ma, Y. Bai, Q. Chen, F. Xiao, K. Sun and H. Zhou, Self-elimination of intrinsic defects improves the low-temperature performance of perovskite photovoltaics, *Joule*, 2020, **4**, 1961–1976.
- 4 H. Min, D. Y. Lee, J. Kim, G. Kim, K. S. Lee, J. Kim, M. J. Paik, Y. K. Kim, K. S. Kim, M. G. Kim, T. J. Shin and S. Il Seok, Perovskite solar cells with atomically coherent interlayers on SnO<sub>2</sub> electrodes, *Nature*, 2021, **598**, 444–450.
- 5 W. Zhu, W. Chai, D. Chen, J. Ma, D. Chen, H. Xi, J. Zhang, C. Zhang and Y. Hao, High-efficiency (> 14%) and air-stable carbon-based, all-inorganic CsPbI<sub>2</sub>Br perovskite solar cells through a top-seeded growth strategy, *ACS Energy Lett.*, 2021, **6**, 1500–1510.
- 6 M. Jeong, I. W. Choi, E. M. Go, Y. Cho, M. Kim, B. Lee, S. Jeong, Y. Jo, H. W. Choi, J. Lee, J.-H. Bae, S. K. Kwak, D. S. Kim and C. Yang, Stable perovskite solar cells with efficiency exceeding 24.8% and 0.3 V voltage loss, *Science*, 2020, **369**, 1615–1620.
- 7 N. Arora, M. I. Dar, A. Hinderhofer, N. Pellet, F. Schreiber, S. M. Zakeeruddin and M. Grätzel, Perovskite solar cells with CuSCN hole extraction layers yield stabilized efficiencies greater than 20%, *Science*, 2017, **358**, 768–771.
- 8 H. Zhang, J. Xiao, J. Shi, H. Su, Y. Luo, D. Li, H. Wu, Y.-B. Cheng and Q. Meng, Self-adhesive macroporous carbon electrodes for efficient and stable perovskite solar cells, *Adv. Funct. Mater.*, 2018, **28**, 1802985.
- 9 Y. Rong, Y. Hu, A. Mei, H. Tan, M. I. Saidaminov, S. Il Seok, M. D. McGehee, E. H. Sargent and H. Han, Challenges for commercializing perovskite solar cells, *Science*, 2018, **361**, 6408.
- 10 C. Zhang, S. Liang, W. Liu, F. T. Eickemeyer, X. Cai, K. Zhou, J. Bian, H. Zhu, C. Zhu, N. Wang, Z. Wang, J. Zhang, Y. Wang, J. Hu, H. Ma, C. Xin, S. M. Zakeeruddin, M. Grätzel and Y. Shi, Ti<sub>1</sub>-graphene single-atom material for improved energy level alignment in perovskite solar cells, *Nat. Energy*, 2021, **6**, 1154–1163.
- 11 T. Ye, Y. Hou, A. Nozariasbmarz, D. Yang, J. Yoon, L. Zheng, K. Wang, K. Wang, S. Ramakrishna and S. Priya, Cost-effective high-performance charge-carrier-transport-layer-free perovskite solar cells achieved by suppressing ion migration, *ACS Energy Lett.*, 2021, **6**, 3044–3052.
- 12 C. Zhang, S. Wang, H. Zhang, Y. Feng, W. Tian, Y. Yan, J. Bian, Y. Wang, S. Jin, S. M. Zakeeruddin, M. Grätzel and Y. Shi, Efficient stable graphene-based perovskite solar cells with high flexibility in device assembling *via* modular architecture design, *Energy Environ. Sci.*, 2019, **12**, 3585–3594.
- 13 Y. Zhu, S. Jia, J. Zheng, Y. Lin, Y. Wu and J. Wang, Facile synthesis of nitrogen-doped graphene frameworks for enhanced performance of hole transport material-free perovskite solar cells, *J. Mater. Chem. C*, 2018, **6**, 3097–3103.
- 14 Z. Wu, Z. Liu, Z. Hu, Z. Hawash, L. Qiu, Y. Jiang, L. K. Ono and Y. Qi, Highly efficient and stable perovskite solar cells *via* modification of energy levels at the perovskite/carbon electrode interface, *Adv. Mater.*, 2019, **31**, 1804284.
- 15 Y. Wu, H. Zhu, B.-B. Yu, S. Akin, Y. Liu, Z. Shen, L. Pan and H. Cai, Interface modification to achieve high-efficiency and stable perovskite solar cells, *Chem. Eng. J.*, 2022, **433**, 134613.
- 16 Q. Jiang, Y. Zhao, X. Zhang, X. Yang, Y. Chen, Z. Chu, Q. Ye, X. Li, Z. Yin and J. You, Surface passivation of perovskite film for efficient solar cells, *Nat. Photonics*, 2019, **13**, 460–466.
- 17 S. You, H. Zeng, Z. Ku, X. Wang, Z. Wang, Y. Rong, Y. Zhao, X. Zheng, L. Luo, L. Li, S. Zhang, M. Li, X. Gao and X. Li, Multifunctional polymer-regulated SnO<sub>2</sub> nanocrystals enhance interface contact for efficient and stable planar perovskite solar cells, *Adv. Mater.*, 2020, **32**, 2003990.
- 18 C. Zhang, H. Wang, H. Li, Q. Zhuang, C. Gong, X. Hu, W. Cai, S. Zhao, J. Chen and Z. Zang, Simultaneous passivation of bulk and interface defects through synergistic effect of anion and cation toward efficient and stable planar perovskite solar cells, *J. Energy Chem.*, 2021, **63**, 452–460.
- 19 Z.-W. Gao, Y. Wang, H. Liu, J. Sun, J. Kim, Y. Li, B. Xu and W. C. H. Choy, Tailoring the interface in FAPbI<sub>3</sub> planar perovskite solar cells by imidazole-graphene-quantum-dots, *Adv. Funct. Mater.*, 2021, **31**, 2101438.
- 20 Z. Liu, K. Deng, J. Hu and L. Li, Coagulated SnO<sub>2</sub> colloids for high-performance planar perovskite solar cells with

- negligible hysteresis and improved stability, *Angew. Chem., Int. Ed.*, 2019, **131**, 11621–11628.
- 21 L. Yang, J. Feng, Z. Liu, Y. Duan, S. Zhan, S. Yang, K. He, Y. Li, Y. Zhou, N. Yuan, J. Ding and S. Liu, Record-efficiency flexible perovskite solar cells enabled by multifunctional organic ions interface passivation, *Adv. Mater.*, 2022, **34**, 2201681.
  - 22 Q. Lou, Y. Han, C. Liu, K. Zheng, J. Zhang, X. Chen, Q. Du, C. Chen and Z. Ge,  $\pi$ -conjugated small molecules modified SnO<sub>2</sub> layer for perovskite solar cells with over 23% efficiency, *Adv. Energy Mater.*, 2021, **11**, 2101416.
  - 23 Y. Huang, H. Zhong, W. Li, D. Cao, Y. Xu, L. Wan, X. Zhang, X. Zhang, Y. Li, X. Ren, Z. Guo, X. Wang, D. Eder and S. Wang, Bifunctional ionic liquid for enhancing efficiency and stability of carbon counter electrode-based MAPbI<sub>3</sub> perovskites solar cells, *Sol. Energy*, 2022, **231**, 1048–1060.
  - 24 P.-Y. Gu, N. Wang, A. Wu, Z. Wang, M. Tian, Z. Fu, X. Sun and Q. Zhang, An azaacene derivative as promising electron-transport layer for inverted perovskite solar cells, *Chem. – Asian J.*, 2016, **11**, 2135–2138.
  - 25 G. Xu, C. Xu, L. Chen, J. Ye, J. Dong, Y. Zhong, F. Li, X. He, Y. Yao, J. You and Q. Song, Interface barrier strategy for perovskite solar cells realized by In-situ synthesized poly-ionic layer, *Chem. Eng. J.*, 2022, **439**, 135704.
  - 26 X. Gong, L. Guan, Q. Li, Y. Li, T. Zhang, H. Pan, Q. Sun, Y. Shen, C. Grätzel, S. M. Zakeeruddin, M. Grätzel and M. Wang, Black phosphorus quantum dots in inorganic perovskite thin films for efficient photovoltaic application, *Sci. Adv.*, 2020, **6**, eaay5661.
  - 27 M. Kim, J. Jeong, H. Lu, T. K. Lee, F. T. Eickemeyer, Y. Liu, I. W. Choi, S. J. Choi, Y. Jo, H.-B. Kim, S.-I. Mo, Y.-K. Kim, H. Lee, N. G. An, S. Cho, W. R. Tress, S. M. Zakeeruddin, A. Hagfeldt, J. Y. Kim, M. Grätzel and D. S. Kim, Conformal quantum dot–SnO<sub>2</sub> layers as electron transporters for efficient perovskite solar cells, *Science*, 2022, **375**, 302–306.
  - 28 J. Chen, X. Zhao, S.-G. Kim and N.-G. Park, Multifunctional chemical linker imidazoleacetic acid hydrochloride for 21% efficient and stable planar perovskite solar cells, *Adv. Mater.*, 2019, **31**, 1902902.
  - 29 L. Zhu, X. Zhang, M. Li, X. Shang, K. Lei, B. Zhang, C. Chen, S. Zheng, H. Song and J. Chen, Trap state passivation by rational ligand molecule engineering toward efficient and stable perovskite solar cells exceeding 23% efficiency, *Adv. Energy Mater.*, 2021, **11**, 2100529.
  - 30 Q. Zhou, D. He, Q. Zhuang, B. Liu, R. Li, H. Li, Z. Zhang, H. Yang, P. Zhao, Y. He, Z. Zang and J. Chen, Revealing steric-hindrance-dependent buried interface defect passivation mechanism in efficient and stable perovskite solar cells with mitigated tensile stress, *Adv. Funct. Mater.*, 2022, **32**, 2205507.
  - 31 Z. Xing, S. Lin, X. Meng, T. Hu, D. Li, B. Fan, Y. Cui, F. Li, X. Hu and Y. Chen, A highly tolerant printing for scalable and flexible perovskite solar cells, *Adv. Funct. Mater.*, 2021, **31**, 2107726.
  - 32 H. Wang, F. Li, P. Wang, R. Sun, W. Ma, M. Chen, W. Miao, D. Liu and T. Wang, Chlorinated fullerene dimers for interfacial engineering toward stable planar perovskite solar cells with 22.3% efficiency, *Adv. Energy Mater.*, 2020, **10**, 2000615.
  - 33 D. He, T. Zhou, B. Liu, L. Bai, W. Wang, H. Yuan, C. Xu, Q. Song, D. Lee, Z. Zang, L. Ding and J. Chen, Interfacial defect passivation by novel phosphonium salts yields 22% efficiency perovskite solar cells: Experimental and theoretical evidence, *EcoMat*, 2022, **4**, e12158.
  - 34 Z.-L. Diao, Y.-W. Zhang, J.-Y. Chen, W.-Y. Tan, Y.-N. Qian, L.-G. Xiao and Y. Min, High-performance blue perovskite light-emitting diodes enabled by a sacrificial agent maleic anhydride, *J. Phys. Chem. C*, 2022, **126**, 6153–6160.
  - 35 Y. Dong, W. Shen, W. Dong, C. Bai, J. Zhao, Y. Zhou, F. Huang, Y.-B. Cheng and J. Zhong, Chlorobenzenesulfonic potassium salts as the efficient multifunctional passivator for the buried interface in regular perovskite solar cells, *Adv. Energy Mater.*, 2022, **12**, 2200417.
  - 36 Z. Xiong, X. Chen, B. Zhang, G. O. Odunmbaku, Z. Ou, B. Guo, K. Yang, Z. Kan, S. Lu, S. Chen, N. A. N. Ouedraogo, Y. Cho, C. Yang, J. Chen and K. Sun, Simultaneous interfacial modification and crystallization control by biguanide hydrochloride for stable perovskite solar cells with PCE of 24.4%, *Adv. Funct. Mater.*, 2022, **34**, 2106118.
  - 37 X. Zhang, D. Zhang, Y. Zhou, Y. Du, J. Jin, Z. Zhu, Z. Wang, X. Cui, J. Li, S. Wu, J. Zhang and Q. Tai, Fluorinated interfaces for efficient and stable low-temperature carbon-based CsPbI<sub>2</sub>Br perovskite solar cells, *Adv. Funct. Mater.*, 2022, **32**, 2205478.
  - 38 H. Bi, B. Liu, D. He, L. Bai, W. Wang, Z. Zang and J. Chen, Interfacial defect passivation and stress release by multifunctional KPF<sub>6</sub> modification for planar perovskite solar cells with enhanced efficiency and stability, *Chem. Eng. J.*, 2021, **418**, 129375.
  - 39 Y. Liu, W. Xiang, S. Mou, H. Zhang and S. Liu, Synergetic surface defect passivation towards efficient and stable inorganic perovskite solar cells, *Chem. Eng. J.*, 2022, **447**, 137515.
  - 40 D. Cao, W. Li, X. Zhang, L. Wan, Z. Guo, X. Wang, D. Eder and S. Wang, Current state-of-the-art characterization methods for probing defect passivation towards efficient perovskite solar cells, *J. Mater. Chem. A*, 2022, **10**, 19278–19303.
  - 41 H. Bi, X. Zuo, B. Liu, D. He, L. Bai, W. Wang, X. Li, Z. Xiao, K. Sun, Q. Song, Z. Zang and J. Chen, Multifunctional organic ammonium salt-modified SnO<sub>2</sub> nanoparticles toward efficient and stable planar perovskite solar cells, *J. Mater. Chem. A*, 2021, **9**, 3940–3951.
  - 42 T. A. Gundrizer and A. A. Davydov, IR spectra of oxygen adsorbed on SnO<sub>2</sub>, *React. Kinet. Catal. Lett.*, 1975, **3**, 63–70.
  - 43 H. Zhong, W. Li, Y. Huang, D. Cao, C. Zhang, H. Bao, Z. Guo, L. Wan, X. Zhang, X. Zhang, Y. Li, X. Ren, X. Wang, D. Eder, K. Wang, S. Liu and S. Wang, All-inorganic perovskite solar cells with tetrabutylammonium acetate as the buffer layer between the SnO<sub>2</sub> electron transport film and CsPbI<sub>3</sub>, *ACS Appl. Mater. Interfaces*, 2022, **14**, 5183–5193.
  - 44 Z. Li, J. Feng, J. Cao, J. Jin, Y. Zhou, D. Cao, Z. Liang, B. Zhu, M. Li, L. Zhao and S. Wang, New carbon nitride C<sub>3</sub>N<sub>3</sub>

- additive for improving cationic defects of perovskite solar cells, *Energy Environ. Mater.*, 2022, **6**, e12283.
- 45 P. Li, C. Liang, Y. Zhang, F. Li, Y. Song and G. Shao, Polyethyleneimine high-energy hydrophilic surface interfacial treatment toward efficient and stable perovskite solar cells, *ACS Appl. Mater. Interfaces*, 2016, **8**, 32574–32580.
- 46 P. Fu, L. Huang, W. Yu, D. Yang, G. Liu, L. Zhou, J. Zhang and C. Li, Efficiency improved for inverted polymer solar cells with electrostatically self-assembled BenMeIm-Cl ionic liquid layer as cathode interface layer, *Nano Energy*, 2015, **13**, 275–282.
- 47 Y. Han, H. Zhao, C. Duan, S. Yang, Z. Yang, Z. Liu and S. Liu, Controlled n-doping in air-stable CsPbI<sub>2</sub>Br perovskite solar cells with a record efficiency of 16.79%, *Adv. Funct. Mater.*, 2020, **30**, 1909972.
- 48 J. Zhuang, P. Mao, Y. Luan, N. Chen, X. Cao, G. Niu, F. Jia, F. Wang, S. Cao and J. Wang, Rubidium fluoride modified SnO<sub>2</sub> for planar n-i-p perovskite solar cells, *Adv. Funct. Mater.*, 2021, **31**, 2010385.
- 49 Y. Li, L. Meng, Y. Yang, G. Xu, Z. Hong, Q. Chen, J. You, G. Li, Y. Yang and Y. Li, High-efficiency robust perovskite solar cells on ultrathin flexible substrates, *Nat. Commun.*, 2016, **7**, 10214.
- 50 M. Sendner, P. K. Nayak, D. A. Egger, S. Beck, C. Müller, B. Epding, W. Kowalsky, L. Kronik, H. J. Snaith, A. Pucci and R. Lovrinčić, Optical phonons in methylammonium lead halide perovskites and implications for charge transport, *Mater. Horiz.*, 2016, **3**, 613–620.
- 51 D. Yang, R. Yang, K. Wang, C. Wu, X. Zhu, J. Feng, X. Ren, G. Fang, S. Priya and S. Liu, High efficiency planar-type perovskite solar cells with negligible hysteresis using EDTA-complexed SnO<sub>2</sub>, *Nat. Commun.*, 2018, **9**, 3239.
- 52 W. Zhao, P. Guo, J. Su, Z. Fang, N. Jia, C. Liu, L. Ye, Q. Ye, J. Chang and H. Wang, Synchronous passivation of defects with low formation energies *via* terdentate anchoring enabling high performance perovskite solar cells with efficiency over 24%, *Adv. Funct. Mater.*, 2022, **32**, 2200534.